

Interpolation of the Mean Anomalies for Cloud Filling in Land Surface Temperature and Normalized Difference Vegetation Index

Ana F. Militino¹, M. Dolores Ugarte¹, Unai Pérez-Goya¹, and Marc G. Genton²

Abstract—When monitoring time series of remote sensing data, it is advisable to fill gaps, i.e., missing or distorted data, caused by atmospheric effects or technical failures. In this paper, a new method for filling these gaps called interpolation of the mean anomalies (IMA) is proposed and compared with some competitors. The method consists of: 1) defining a neighborhood for the target image from previous and subsequent images across previous and subsequent years; 2) computing the mean target image of the neighborhood; 3) estimating the anomalies in the target image by subtracting the mean image from the target image; 4) filtering the anomalies; 5) averaging the anomalies over a predefined window; 6) interpolating the averaged anomalies; and 7) adding the interpolated anomalies to the mean image. To assess the performance of the IMA method, both a real example and a simulation study are conducted with a time series of Moderate Resolution Imaging Spectroradiometer (MODIS) TERRA and MODIS AQUA images captured over the region of Navarre (Spain) from 2011 to 2013. We analyze the land surface temperature (LST) day and night, and the normalized difference vegetation index (NDVI). In the simulation study, seven sizes of artificial clouds are randomly introduced to each image in the studied time series. The square root of the mean-squared prediction error (RMSE) between the original and the filled data is chosen as an indicator of the goodness of fit. The results show that the IMA method outperforms Timesat, Hants, and Gapfill (GF) in filling small, moderate, and big cloud gaps in both the day and night LST and NDVI data, reaching RMSE reductions of up to 23%.

Index Terms—Geostatistics, moderate resolution imaging spectroradiometer (MODIS), smoothing images, thin-plate splines.

I. INTRODUCTION

REMOVING clouds from satellite imagery is an important and crucial task for reconstructing the history and evolution of many remote sensing data. Although very cloudy

images must be dropped from time series, missing or distorted data in images that are only partially clouded can be filled using series of multitemporal images. Therefore, cloud-filling techniques are frequently used when monitoring features that change over time, such as snow cover [1], [2], vegetation [3], [4], land cover change [5], [6], or forestry [7]. Several procedures have been recently introduced [8]–[12], but some of the most popular, e.g., Timesat [13] based on filtering, Hants [14], [15] based on harmonic analysis of time series, and Gapfill (GF) [16], [17] based on a specific ordering of images and quantile regression, provide free access to users and are easy to run. However, these gap-filling techniques are neither simple nor straightforward.

In this paper, we present a new method for filling the gaps caused by missing or distorted data, called interpolation of the mean anomalies (IMA). This method uses the same neighborhood of the target image than GF to capture the temporal dependence between close images, but GF uses quantile regression over the image ranks for predicting every missing data, while IMA uses this neighborhood to derive the anomalies from the mean image, and interpolate them. The neighborhood frame is defined as the set of previous and subsequent images in time periods and years, accommodating the temporal dependence between near images, in the same or different years. In IMA, anomalies in the target image are derived from the mean, and averaged over a predefined window after trimming the extreme values. Next, the method interpolates the averaged anomalies in the original resolution over the study region with thin-plate splines (Tps). These interpolated anomalies are added to the mean image to fill in the gaps. The flowchart in Fig. 1 summarizes the IMA process for one image.

In this paper, we choose bivariate Tps as the interpolator, because of its simplicity and well-known properties [18]. It is frequently used to calibrate, enhance, or improve the quality of remote sensing data [19]–[21], though other interpolators are also available [22], [23]. The bivariate thin-plate spline has the advantage that it can be recast as a kriging method with the trend of the first order, and the generalized covariance function, $\Sigma(d) = |d|^2 \log(d)$, where d is the Euclidean distance [24], [25]. However, Tps does not need to estimate the variogram parameters as kriging. Nevertheless, it provides similar performance [18] based on the principle that nearby observations tend to be more alike [26].

Manuscript received November 9, 2018; revised March 4, 2019; accepted March 5, 2019. Date of publication April 16, 2019; date of current version July 22, 2019. This work was supported in part by project MTM2017-82553-R (AEI/FEDER, UE), in part by projects PI015-2016 and PI043-2017 (Government of Navarra, Spain), and in part by the Fundación CAN-Obra Social Caixa-UNED Pamplona 2016 and 2017. (Corresponding author: Ana F. Militino.)

A. F. Militino, M. D. Ugarte, and U. Pérez-Goya are with the Department of Statistics, Computer Science and Mathematics, Public University of Navarra, 31006 Pamplona, Spain, and also with InaMat, Public University of Navarra, 31006 Pamplona, Spain (e-mail: militino@unavarra.es).

M. G. Genton is with the Computer, Electrical and Mathematical Sciences and Engineering Division (CEMSE), King Abdullah University Science and Technology (KAUST), Thuwal 23955-6900, Saudi Arabia.

Color versions of one or more of the figures in this paper are available online at <http://ieeexplore.ieee.org>.

Digital Object Identifier 10.1109/TGRS.2019.2904193

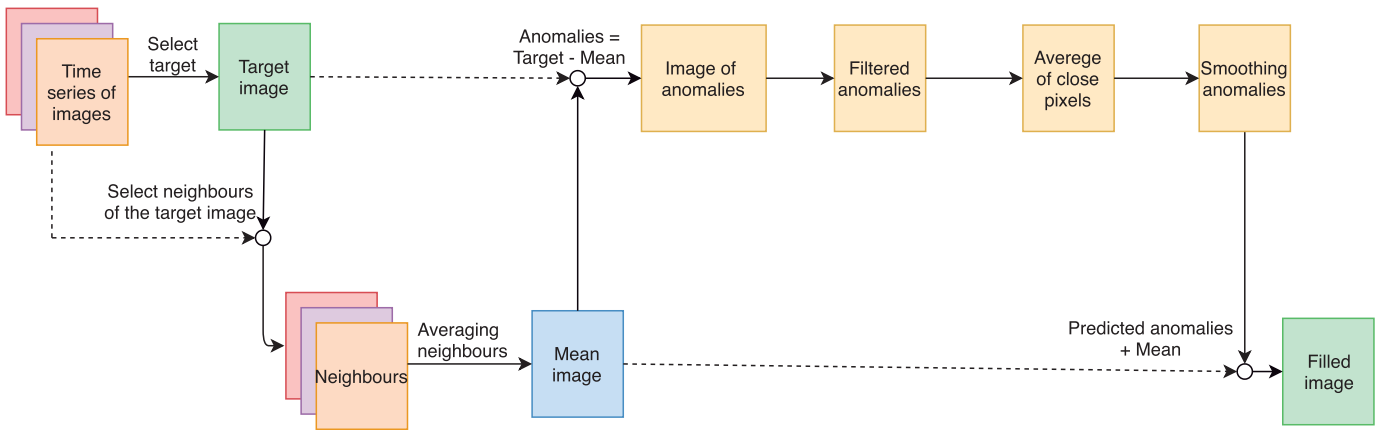


Fig. 1. Flowchart of IMA for processing one image.

The idea of using kriging methods to recover gaps in satellite images is not new. In the past, an indicator kriging was used to fill Landsat images from Mexico [27]. In that study, the author used a kriging method, but the focus of the paper was on calculating the probability that a pixel would be properly classified as obscure or missing remote sensing data, rather than on filling gaps.

Several studies have shown the benefits of using geostatistical methods, over mathematical ones, for filling gaps in satellite imagery. Geostatistical methods explicitly assume that the stochastic spatial dependence inherent in spatial data decreases with distance. For example, Addink [28] made a comparison of the conventional mathematical and the geostatistical methods to replace clouded pixels in NOAA-AVHRR images. The conventional method is maximum value composition (MVC) and the geostatistical methods are kriging and cokriging. The geostatistical methods performed better than those ignoring stochastic spatial dependence, though cokriging methods have computing restrictions when applied to large data sets. Some years later, another study compared noise-reduction NDVI model-based methods [29]. In this case, the authors showed that the double logistic (DL) and asymmetric Gaussian (AG) function-fitting methods of Timesat outperformed the other four alternatives: 4253H [30], twice filter [30], mean-value iteration filter [31], and ARMD3-ARMA5 filter [32].

The effectiveness of Hants was evaluated [33] by reconstructing the spatial patterns of normalized difference vegetation index (NDVI) time series, and other land surface variables, but only the accuracy of the procedure with regard to Moderate Resolution Imaging Spectroradiometer (MODIS) products was shown. Another stochastic approach [34] on spatio-temporal modeling is based on generalized additive models. The application is helpful for situations with high percentages of missing data, but it needs specific programming, and it is very slow when managing large amounts of data.

In response to the 2003 failure of the scan-line corrector (SLC) of the Landsat 7 enhanced thematic mapper plus (ETM+), some filling gap contributions were developed. For example, the neighborhood similar pixel interpolator (NSPI) [35] was proposed for the aim of filling gaps in satellite imagery. NSPI was later improved using geostatistical

techniques [36], [37] and the direct sampling method [38]. Other relevant contributions for filling gaps include the use of differential equations [39], and the estimation of phenological parameters [40]. The success of these models was dependent on tuning some parameters according to the number of annual growing seasons. Geostatistical procedures were also recently compared with direct sampling and weighted regression for cloud filling in Landsat 7 [41].

Another study [42] compared a variety of approaches to filling the gaps in time series of vegetation parameters. A Fourier-based approach, a DL model, an iterative interpolation for data reconstruction, the Whittaker smoother, the Savitzky–Golay (SG) filter, and the locally adjusted cubic spline capping were compared, where cubic spline capping is the best for gap filling [43]. The authors used the historical mean over the past 15 years as a benchmark, and they compared random pixels with this reference, instead of the real observed variable.

In this paper, the performance of IMA is checked with regard to five alternatives: Hants, GF, and three versions of Timesat in both a real example and a simulation study. Fig. 2 shows the flowchart of the simulation study. In the first step, we download the time series of the three variables: 72 composite images of NDVI, 138 composite images of daytime land surface temperature (LST), and 138 nighttime LST captured from MODIS [44] in the Spanish region of Navarre between 2011 and 2013. Second, we define the seven sizes (A, B, C, D, E, F, G) of the artificial clouds randomly introduced to each image in the time series. Third, we run the five aforementioned alternatives of cloud-filling methods and IMA. Fourth, we calculate the root of the mean-squared prediction error (RMSE) for each gap, and finally, we average the RMSE by year and method in each remote sensing data, and we explain the conclusions using a collection of plots and tables.

This paper is organized as follows. Section II describes the MODIS data to be used in this paper. Section III provides the explanation of the new IMA method, and a summary of some popular free access alternatives: Hants, Timesat, and GF. It includes several sections for describing its main features and requirements. Section IV presents the results obtained in the simulation study. Comparisons are made by plotting the square root of the mean-squared prediction error for each variable

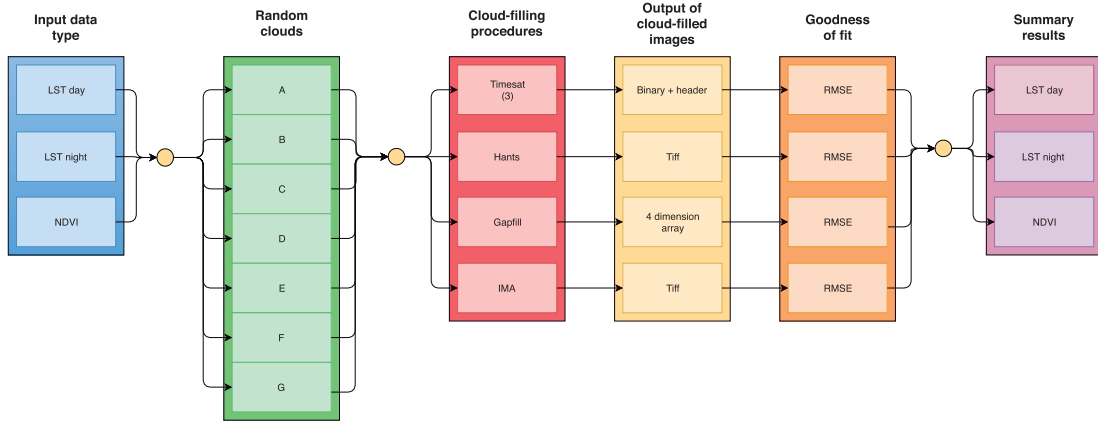


Fig. 2. Flowchart for the simulation study.

versus the size of the introduced random clouds. Section V illustrates the IMA procedure with real data. Section VI provides a discussion, and finally, Section VII ends with the conclusions.

II. MODIS DATA

Frequently, many raw satellite images are almost unusable, because atmospheric disturbances and electronic radiation from the satellites can distort, blur, or degrade the information. The MODIS [44] provides time series of preprocessed series of images, where these effects have been mitigated. In addition, image transformations are made to provide very popular remote sensing data, such as NDVI or LST to the users. These time series of images are already enhanced by composing preprocessed images every 8 or 16 days, and they are available for free. We retrieved remote sensing data from the MODIS instrument in TERRA and AQUA satellites. NDVI images are of 16 day temporal resolution, then only 23 images are available each year in TERRA, and the same number in AQUA. To adjust the balance with the same number of images every month, we get 23 images from Version 5-MYD13A2 (AQUA), and we retrieve an additional image from Version-5 MOD13A2 (TERRA) in November, yet this is not a prerequisite for running IMA.

The NDVI reflects vegetation vigor and it is closely related to the amount of photosynthetically absorbed active radiation as indicated in [45] and [46]. It is calculated through the radiometric information obtained for the red (R) and near-infrared (NIR) wavelengths of the electromagnetic spectrum. Then, the index is defined as $NDVI = ((NIR) - R) / ((NIR) + R)$ [47], and takes values between 0 and 1 with high variability [48].

The LST images of MODIS are derived from the two thermal infrared (TIR) band channels, 31 (10.78–11.28 μm) and 32 (11.77–12.27 μm) [49]. The atmospheric effects are corrected with the split-window algorithm [50], [51]. The algorithm also uses the MODIS Land Cover product (MOD12C1) for correcting the emissivity effects. Composite LST every 8 days is downloaded from Version-5 MOD11A2 and they correspond to the 8 days average LSTs of the Version-5 MOD11A1 product. In all variables, we cropped the H17–V4 MODIS tile containing Navarre, to fit the study

TABLE I

REMOTE SENSING DATA (DATA), CS, CV, MINIMUM, QUANTILES AND MAXIMA OF THE DAY AND NIGHT LST, AND NDVI BY CS IN THE NAVARRE TILE (SPAIN), FROM 2011–2013

Data	CS	CV	Min	1st Q.	Med	3rdQ.	Max
LST Day	DJF	0.015	252.2	279	281.3	283.5	297.5
	MAM	0.020	254.3	288.8	292.9	296.4	314.9
	JJA	0.019	265.9	298.0	302.0	307.0	320.4
	SON	0.028	251.2	285.5	290.7	297.5	314.0
LST Night	DJF	0.012	247.2	272.4	274.3	275.9	288.5
	MAM	0.015	249.2	277.3	280.3	283	293.3
	JJA	0.012	264.0	285.9	288.4	290.6	297.7
	SON	0.018	256.9	278.6	282.1	285.5	294.6
NDVI	DJF	0.33	0	0.36	0.48	0.60	0.95
	MAM	0.29	0	0.48	0.60	0.70	0.95
	JJA	0.40	0	0.36	0.58	0.78	0.98
	SON	0.39	0	0.34	0.52	0.70	0.98

region. This region consists of a 156×145 (22620 pixels) rectangular array, where each pixel corresponds to 1 km^2 (see Fig. 3).

Table I shows the study variables, the climatological seasons (CS) [winter (December, January, and February), spring (March, April, and May), summer (June, July, and August) and fall (September, October, and November)], the coefficient of variation (CV), the minimum, the first, second, and third quartiles, and the maximum of the daytime LST, nighttime LST and NDVI variables in the study region from 2011 to 2013. LST day and night are given in Kelvin degrees, and NDVI has no units with a restricted range between 0 and 0.98. NDVI has greater variability than LST in the four CS.

III. CLOUD-FILLING METHODS

A. Interpolation of the Mean Anomalies Method

We assume that the target image is an LST image, named LST_day_2011.073, which corresponds to the 8 day composite image of March 13, 2011, over Navarre, Spain (see Fig. 3), although any other time period or variable can also be chosen.

This image is represented by the vector $\mathbf{z}_{s t_0} = \{z_{s_i t_0} | i = 1, \dots, m\}$, where $z_{s_i t_0}$ is the remote sensing data observed at location s_i , $s_i \in \mathbf{s} = (s_1, \dots, s_m)$; $m = 22620$ is the total number of pixels in the image, and t_0 is the target time period. Note that m can include pixels of missing data.

The IMA method consists of the next seven steps.

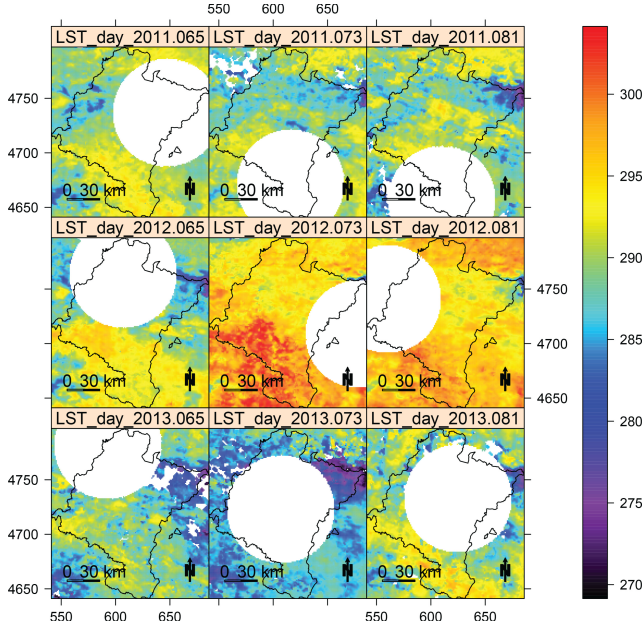


Fig. 3. Example of the neighborhood of the target image LST_day 2011_073 (color bar units in Kelvin degrees) used in the IMA and GF methods, where random gaps of size G have been introduced into every image of the neighborhood. The target image corresponds to March 13, 2011.

1) Define the neighborhood of the target image. The neighborhood $\{z_{s_{t_k}} | t_k = 1, \dots, T_0\}$ of the target image $z_{s_{t_0}}$, consists of the target image, and the preceding and following images in that year, as well as images from those dates during the previous and subsequent years. If the image belongs to the first or last year of the study period, we can choose more subsequent or preceding years, as it is done in this example. Here, the time series are made of 8 day composite images of daytime LST data collected from 2011 to 2013. Therefore, the neighborhood of the target image, including this image has $T_0 = 9$ images, which are identified by the year and Julian day on which they were preprocessed: $I_1 = 2011.065$, $I_2 = 2011.073$, $I_3 = 2011.081$, $I_4 = 2012.065$, $I_5 = 2012.073$, $I_6 = 2012.081$, $I_7 = 2013.065$, $I_8 = 2013.073$, and $I_9 = 2013.081$ (see Fig. 3 for details). We use the same neighborhood whether the target image is $I_2 = 2011.073$, $I_5 = 2012.073$, or $I_8 = 2013.073$ since this paper only includes data from 2011 to 2013.

The size and dimension of this neighbor can be enlarged according to the availability, the quality of satellites images, and the repetitive cloudiness.

2) Compute the mean target image of the neighborhood. We assign to each pixel, the mean of the nonempty pixels at the same location of the neighbor images. Thus, the mean target image is given by $\bar{z}_{s_{t_0}} = \{\bar{z}_{s_{t_0}} | i = 1, \dots, m\}$, where

$$\bar{z}_{s_{t_0}} = \frac{\sum_{t_k=1}^{T_0} z_{s_{t_k}}}{T_0} \quad (1)$$

where $z_{s_{t_k}}$ is the i th observed pixel of the t_k period in the neighborhood of the target image.

3) Estimate the anomalies of the target image by subtracting the mean image from the target image. In other words, $w_{s_{t_0}} = z_{s_{t_0}} - \bar{z}_{s_{t_0}}$ is the target image of the anomalies, and

$w_{s_{t_j}} = \{w_{s_{t_j}} | i = 1, \dots, m\}$, where

$$w_{s_{t_j}} = z_{s_{t_j}} - \bar{z}_{s_{t_0}}, \quad \text{for } i = 1, \dots, m. \quad (2)$$

4) Filter the anomalies. The target anomalies are filtered out by removing the upper and lower 5% of the extreme values, i.e., percentiles ($p_{0.95}$) and ($p_{0.05}$), respectively. Removing extreme anomalies prevents from distorted data still present in some images. This step follows the expression:

$$w'_{s_{t_0}} = \begin{cases} w_{s_{t_0}}, & \text{if } p_{0.05}(w_{s_{t_0}}) < (w_{s_{t_0}}) < p_{0.95}(w_{s_{t_0}}) \\ \text{non value,} & \text{otherwise} \end{cases}$$

for $i = 1, \dots, m_1$. Filtering the target anomalies reduces the maximum total number of pixels in the tile from $m = 22620$ to $m_1 = 20358$. Alternative threshold values of filtering may be used depending on the quality of the input images, yet these percentiles are recommended.

5) Average the anomalies over a predefined window. The anomalies are averaged over their neighboring pixels in a window of 5×5 pixels, when the spatial resolution is 1 km^2 . We assign the mean of the nonempty anomalies in the same window to all the pixels of the window. Unless all the anomalies in the same window have missing data, we will reduce the number of missing pixels. There are three benefits gained by performing this step: we avoid sudden changes among close pixels, we reduce the number of empty anomalies, and we reduce the number of the equations to be solved when using Tps. Therefore, a good tradeoff between computing time and prediction error is achieved. Removing sudden changes among close pixels is especially important in NDVI images, because these remote sensing data are very sensitive to small changes in vegetation, sensor calibration, and atmospheric correction. Alternative shrinking factors can also be used, depending on the image resolution and computing capacities. Here, we have chosen a factor equal to 5 because the spatial dependence in these variables is about 5 km^2 , yet it can be changed. Then, the averaged anomalies are defined as

$$w''_{s_{t_0}} = \frac{\sum_{s_i \in T_1} w'_{s_{t_0}}}{25} \quad (3)$$

where $i = 1, \dots, n$, T_1 is a 5×5 pixel window around s_i . This step further reduces the m_1 maximum number of pixels in the target image to $n = m_1/25 \approx 928$ pixels.

6) Interpolate the averaged anomalies. We choose bivariate thin-plate splines to interpolate the target image of the averaged anomalies because of its well-known properties [52], yet other alternatives can be used [53]. The thin-plate spline model provides a flexible relationship between the anomalies $w''_{s_{t_0}} = (w''_{s_{t_0}}, \dots, w''_{s_{n,t_0}})$, and the the planar coordinates (x_s, y_s) . Predictions are given by $\hat{w}''_{s_{t_0}} = \sum_{j=1}^3 a_j p_j(s_i) + \sum_{i=1}^n b_i \phi(d)$, where $\phi(d) = d^2 \log(d)$ is a basis function, d is the Euclidean distance between the prediction location s_0 and each data location s_i , and $p_1(s_i) = 1$, $p_2(s_i) = x$, $p_3(s_i) = y$. The weights $\{a_j | j = 1, 2, 3\}$ and $\{b_i | i = 1, \dots, n\}$ are estimated by solving a linear system of order n [54]–[56]. The predictions are obtained over the m pixels of the target image.

This process is nowadays programmed in mathematical, remote sensing, and statistical software in a very efficient way.

TABLE II

NUMBER OF FILLED IMAGES FOR THE THREE REMOTE SENSING DATA (LST DAY, LST NIGHT, AND NDVI), TIME PERIODS, YEARS, CLOUD SIZES, AND METHODS (HANTS, THREE TIMESAT, GF, AND IMA) USED IN THE SIMULATION STUDY

	LST Day	LST Night	NDVI
Time periods by year	46	46	24
Years	3	3	3
Cloud Sizes	7	7	7
Number of methods	6	6	6
Total	5,796	5,796	3,024
Total of 14,616 filled images			

Here, we use the R package `fields` [57], where uncertainty measures can also be derived.

7) Add the interpolated anomalies to the mean image. Thus, the final predicted image is

$$\hat{\mathbf{z}}_{st_0} = \bar{\mathbf{z}}_{st_0} + \hat{\mathbf{w}}''_{st_0}. \quad (4)$$

Finally, we programmed IMA in R; and the code for running IMA is available from the authors.

B. Hants

The Harmonic Analysis of Time Series (Hants) was a procedure originally developed for processing time series of noisy remote sensing data [14], and a few years later, the Hants algorithm was published [15]. The performance of this algorithm has been studied with applications to leaf area index (LAI), LST, and the polarization difference brightness temperature (PDBT) [33]. The application was released as plug-in for the geographical information system (GIS) platform called the Geographic Resources Analysis Support System (GRASS) [58]. The Hants algorithm uses an iterative procedure to fit a curve based on pixel-wise time series separately, but ignores stochastic spatial dependence. The process follows the steps.

- 1) Checking the time series and flag samples outside the valid range of data.
- 2) Fitting the remaining valid samples of the series by several prescribed harmonic components.
- 3) If the maximum signed bias between the fit series and the valid samples is larger than a user-defined threshold, and the number of the remaining samples exceeds the minimum number of samples necessary for the reconstruction process, then it rejects the samples with bias larger than half of the maximum bias and return to step 2). Otherwise, stop the processing.

C. Timesat

Timesat [13] is a software released in 2002 and coded in Matlab and Fortran, yet those are not necessary for running it. It implements three processing methods based on least-squares fits for satellite time series processing: SG filtering, DL, and AG.

The software was designed to analyze satellite time series data from satellites by extracting seasonal parameters from smoothed versions of the data, but it works with pixel-by-pixel time series. Timesat needs a specific image binary

format that can be obtained using the `raster` package of the R software [59]. First, the user must specify the number of rows and columns to be processed (156×145), the type of data (16 bit integer), the range of the variables ($[0-10000]$ for NDVI and $[0-999.9]$ for LST day/night), the lag period length (8 or 15), and the time series length (3 years). These configuration input parameters must be provided using a graphical interface. When exporting the smoothed image, a matrix is produced, which must be completed in order to be exported to R; the `raster` package will help again to convert an *hdr* format into a *Tiff* format.

D. Gapfill

GF is the specific function of the `gapfill` R package [16] that fills missing values of satellite data with the GF method. The method ranks the images preceding and following the target image, and predicts the gap using quantile regression. This regression is an extension of the classical estimation of the conditional mean model to conditional quantile functions, which can be explained as follows:

Let $\mathbf{p} = \{p_{ij}\}$, for $i = 1, \dots, I$ and $j = 1, \dots, J$ be the j th pixel in the i th image and let $\mathbf{r} = \{r_1, \dots, r_I\}$ be the ranks or ordinal sequence of these pixels. Then, instead of estimating the conditional expectation of the response variable \mathbf{p} given the explanatory variable \mathbf{r} , i.e., $E[\mathbf{p}|\mathbf{r}]$, as it is done in classical linear regression, the quantile regression estimates the conditional θ quantile given \mathbf{r} , i.e., $Q_\theta(\mathbf{p}|\mathbf{r})$. Therefore, the θ quantile regression model is defined as

$$Q_\theta(\mathbf{p}|\mathbf{r}) = \beta_0(\theta) + \beta_1(\theta)\mathbf{r} \quad (5)$$

where $\beta_0(\theta)$ and $\beta_1(\theta)$ are the regression coefficients with a similar interpretation of the classical regression model [60]. This algorithm was explained and compared with Timesat for NDVI in a very recent paper [16]. To run GF in our simulation study, we tune the programming to tackle the challenge of filling big gaps. First, in the `Predict` function, we enlarge to 20, the minimum number of nonempty pixels in the target image originally written as `nTargetImage = 5`. Second, in the `rank` function, we add the argument `ties.method = first` for avoiding ties in assigned ranks. Third, we include the code `if(sum(is.na(r)) < 2); return(NA)` to guarantee at least two different ranks for running the quantile regression. When many missing pixels are in the same locations of different images in the same neighborhood, it is not possible to assign ranks.

GF is easily accesible because of its free distribution, and it provides measures of uncertainty through prediction intervals.

IV. SIMULATION RESULTS

The performance of the proposed IMA method for filling clouds in satellite imagery is evaluated in both a real example and a simulation study using 348 images captured over Navarre, Spain, between 2011 and 2013. In the simulation study, IMA is compared with Hants, the three versions of Timesat, and GF. Time series of daytime LST (LST Day), nighttime LST (LST Night), and NDVI is analyzed. The LST time series each contains 138 composite images of 8 day

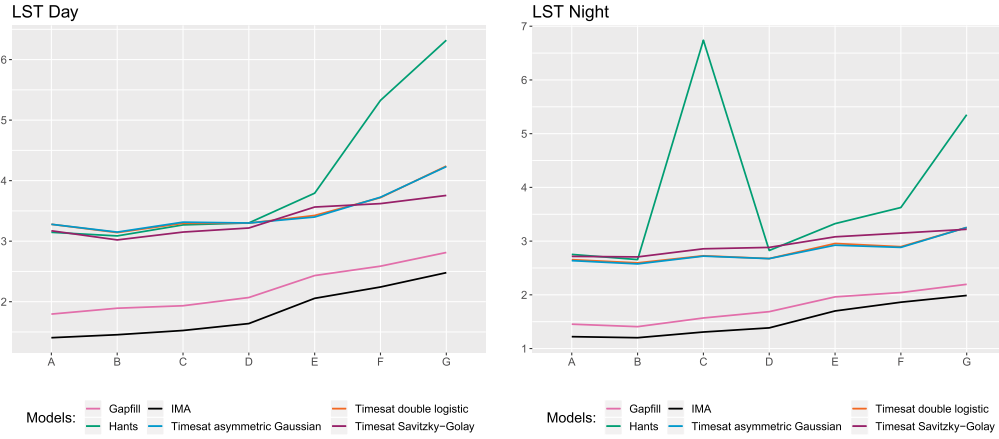


Fig. 4. RMSE versus artificial cloud size for the six models compared in the simulation study with LST day (on the left) and LST night (on the right) images of Navarre, Spain, 2011–2013.

TABLE III
CLOUD SIZE, RADIUS, TOTAL SURFACE, AND MEAN SURFACE PERCENTAGE OF THE DISTORTED IMAGES WITH THE ARTIFICIAL CLOUDS USED IN THE SIMULATION STUDY FOR LST DAY

Cloud size	Radius (<i>km</i>)	Surface (<i>km</i> ²)	Mean Surface (%)
A	15	706.8	5.5
B	17.5	962.1	6.6
C	20	1256.6	7.6
D	30	2827.4	13.0
E	50	7852.9	28.4
F	60	11309.7	37.1
G	70	15393.8	44.4

time periods; the NDVI time series contains 72 composite images of 16 day time periods. In the images of these time series, we introduced artificial clouds of seven different sizes (*A*, *B*, *C*, *D*, *E*, *F*, *G*) to generate missing data inside a randomly located circle. Fig. 3 shows an example of randomly introduced size-*G* clouds. For each of the images of the time series and variables, we run the six cloud-filling methods mentioned above: Hants, three versions of Timesat, GF, and IMA. Table II shows the distribution of the 14616 images used in the simulation study according to the derived variables, the cloud sizes, and the methods. Table III shows the cloud size, the radius, the total surface (calculated as $\pi \times r^2$), and the mean surface percentage of the artificial cloud coverage. The mean surface percentage varies from 6% to 44% depending on the size of the cloud, and how much of the cloud is located inside the tile.

We evaluate the performance of the methods for each size of artificial cloud, each derived variable, and each model. Pixel-by-pixel square differences between the observed and filled data are averaged for calculating the square RMSE. The expression is given by

$$\text{RMSE}(k, l, p) = \sqrt{\frac{\sum_{s_i, t_j} (z_{s_i t_j k l p} - \hat{z}_{s_i t_j k l p})^2}{IT}}$$

$$s_i = 1, \dots, I$$

$$t_j = 1, \dots, T$$

$$k = A, B, C, D, E, F, G$$

$l = \text{LST day, LST night, NDVI, and}$

$p = \{\text{Gapfill, Hants, Timesat AG,}$

$\text{Timesat DL, Timesat SG and IMA}\}, (6)$

where $z_{s_i t_j}$ and $\hat{z}_{s_i t_j}$ are, respectively, the original and predicted values of the remote sensing data, I is the number of pixels inside the cloud gap, T is the number of images, k is the type of cloud, l is the derived variable, and p is the smoothing procedure.

The $\text{RMSE}(k, l, p)$ for the six cloud-filling methods, the seven sizes of artificial clouds, and the three derived variables are shown in Figs. 4 and 5, respectively. The left plot in Fig. 4 exhibits the LST day RMSE. Different lines correspond to different cloud-filling methods. Pink and black colors are for GF and IMA, respectively, while the other colors correspond to Timesat and Hants. In this figure, Hants and the three Timesat versions show similar RMSE values for the small and moderate cloud sizes, though Hants gives the highest RMSE values for the big clouds. Both Hants and Timesat consistently produce higher RMSE values than GF or IMA. IMA clearly outperforms GF regardless of cloud sizes. Similar conclusions are drawn for LST Night (on the right of Fig. 4), where Hants exhibits the highest RMSE values, though not just for big clouds, and IMA always shows the lowest RMSE values for all cloud sizes. Fig. 5 shows the RMSE for NDVI. We observe a similar pattern, but we also note a positive correlation between RMSE and cloud sizes. Hants provides the highest RMSE values for almost all the cloud sizes, and IMA the lowest for all the cloud sizes. RMSE estimates are lower for NDVI than for LST because NDVI is constrained to take values between 0 and 1.

Clearly, GF and IMA outperform the others methods, and therefore, both Tables IV and V focus on the RMSE estimates and the percent of reduction. Shrinking percentages are always in favor of IMA, however, we see in Table IV that these percentages decrease as cloud size increases, because both methods become less efficient as long as the clouds get bigger. In Table V, we see no such inverse correlation between cloud size and reduction percentage, mainly because NDVI is fairly variable and its values are limited between 0 and 1. Extensive simulation studies not shown here for preserving space reveal

TABLE IV
ROOT MEAN SQUARED PREDICTION ERROR OF GF AND IMA, AND REDUCTION PERCENTAGE OBTAINED FROM THE SIMULATION STUDIES OF LST DAY AND LST NIGHT

	RMSE LST Day			RMSE LST Night		
	GF	IMA	Reduction (%)	GF	IMA	Reduction (%)
A	1.80	1.41	21.7	1.46	1.22	16.0
B	1.89	1.45	23.2	1.41	1.21	14.6
C	1.93	1.52	21.1	1.57	1.31	16.7
D	2.07	1.64	20.8	1.69	1.38	17.9
E	2.43	2.06	15.5	1.96	1.70	13.4
F	2.59	2.24	13.3	2.04	1.86	8.8
G	2.81	2.48	11.9	2.20	1.99	9.5

TABLE V
ROOT MEAN SQUARED PREDICTION ERROR OF GF AND IMA, AND REDUCTION PERCENTAGE OBTAINED IN THE SIMULATION STUDY OF NDVI

	RMSE NDVI		
	GF	IMA	Reduction (%)
A	0.051	0.046	8.5
B	0.051	0.048	7.0
C	0.050	0.048	4.4
D	0.063	0.055	12.4
E	0.067	0.060	11.3
F	0.075	0.066	11.7
G	0.082	0.073	11.0

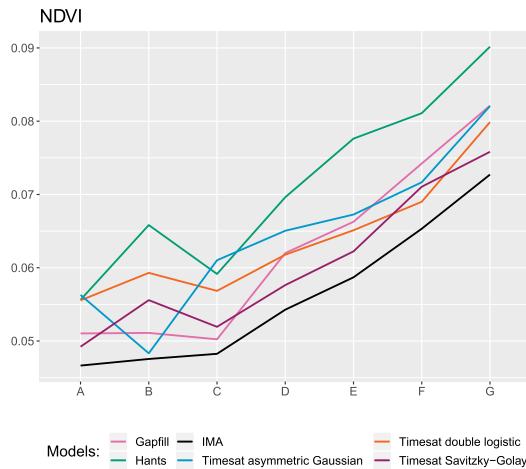


Fig. 5. RMSE versus artificial cloud size for the six models compared in the simulation study with NDVI images of Navarre, Spain, 2011–2013.

that inside a cloud, the pixels closer to the center of the cloud have higher RMSE values than those near the boundary, but the fidelity of the prediction also depends on the similarity of the missing pixels to those from which they borrow information.

Overall, IMA outperforms the three versions of Timesat, Hants, and GF regardless of the cloud size for all three variables, LST Day, LST Night, and NDVI. GF is the closest competitor. Fig. 6 illustrates the filling processes of the six methods when filling the target image LST_2011_073. Coordinates are given in UTM scaled to kilometers. In this example, IMA provides the best filling.

V. RESULTS OF IMA AND GAPFILL PROCEDURES WITH REAL DATA

In addition, we also illustrate the IMA procedure in real data by filling clouds in the LST day and NDVI daily target images

TABLE VI
ROOT MEAN SQUARED PREDICTION ERROR IN THE CLOUD SET OF THE LST DAY AND NDVI IMAGES OF NAVARRE OF THE 16TH (2011 198), 17TH (2011 199), AND 18TH (2011 199) OF JULY 2012 OBTAINED WITH GF AND IMA

Julian Day	Filling cloud Surface km^2	RMSE LST day		RMSE NDVI	
		GF	IMA	GF	IMA
2011198	7332.53	1.58	1.28	0.07	0.07
2011199	12081.15	4.78	1.99	0.08	0.08
2011200	16877.81	4.87	2.03	0.10	0.11
sample mean	12097.16	3.74	1.77	0.08	0.09

of the 16th (2012 198), 17th (2012 199), and 18th (2012 200) of July 2012 in Navarre, Spain. Those days were, in principle, free of clouds, but we mimic cloudy days adding a real cloud mask to the target images.

Daily images are more variable than composite images, because they are only slightly preprocessed. Therefore, for a robust estimation of the anomalies, we need to increase the neighborhood size of the target images. Now, each target image has a neighborhood of 3×7 images corresponding to the three previous and three subsequent images of the same year, and the corresponding images from those dates during the previous and subsequent years. The three target images are consecutive, then the neighborhood is made up of 27 images, and in the end, all the images are filled. The LST day images are daily images retrieved from MOD11A1 (TERRA) Version 5 with a spatial resolution of $1 km^2$. The NDVI images are defined using the red and NIR wavelengths from MOD09GA (TERRA) Version 5 in the same days, because MODIS does not provide NDVI daily images. These images are reprojected for homogeneity reasons to the same resolution of LST day images, because the original resolution is $0.5 km^2$, yet this step is not required in the IMA procedure.

The first row of Fig. 7 shows the observed LST day target images of the 16th (2012 198), 17th (2012 199), and 18th (2012 200) of July 2012. The second row shows the same images masked with real clouds from the 3rd, 14th, and 21st of July 2011. The third row shows the high fidelity of the IMA predicted images to the original target ones. Table VI summarizes the root mean-squared prediction error obtained with IMA and GF in the clouds of the LST day and NDVI target images. Separately and jointly, IMA reduces the root mean-squared prediction error estimated by GF in LST day and it is equally competitive than GF in NDVI images, matching the results of the simulation study. The computing time for processing the raster of the three LST day target images in a PC with an Intel Core i7-4790, and 16 GB of RAM takes about 4 s with IMA, while GF takes 1 h 30 for filling only the gaps of those images.

VI. DISCUSSION

For checking the performance of IMA with regard to the aforementioned gap-filling methods, an extensive simulation study involving the filling process of 14616 LST day and NDVI images in different scenarios was conducted. Every gap-filling method is based on different models and assumptions, becoming difficult a theoretical comparison. Therefore, the

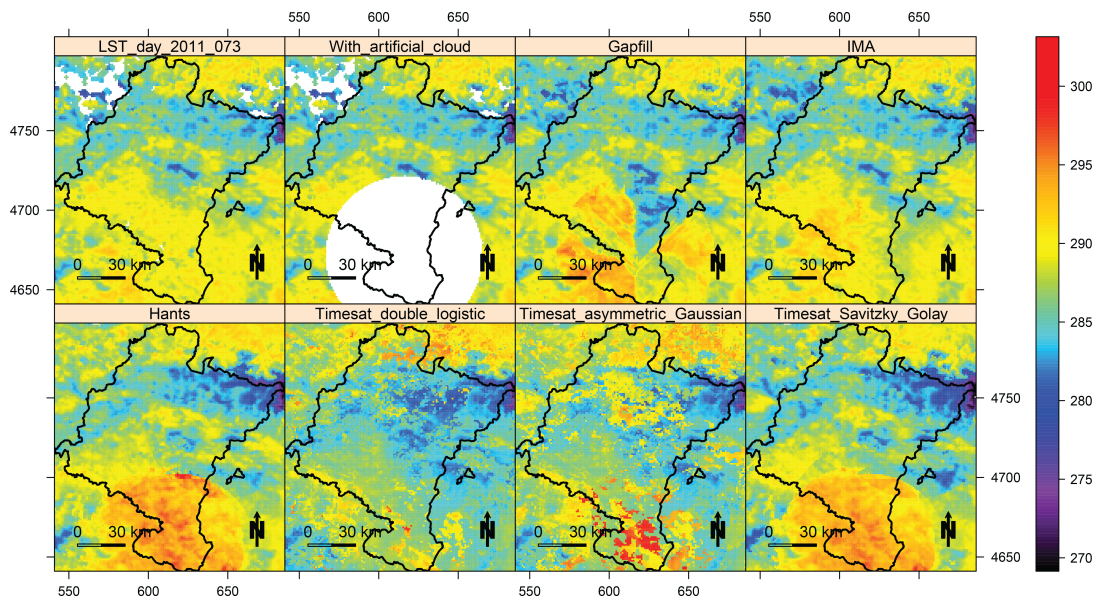


Fig. 6. LST_2011_073 daytime target image, the target image with artificial cloud, and the reconstructed images with GF, IMA, Hants, Timesat DL, Timesat AG, and Timesat SG in Kelvin degrees.

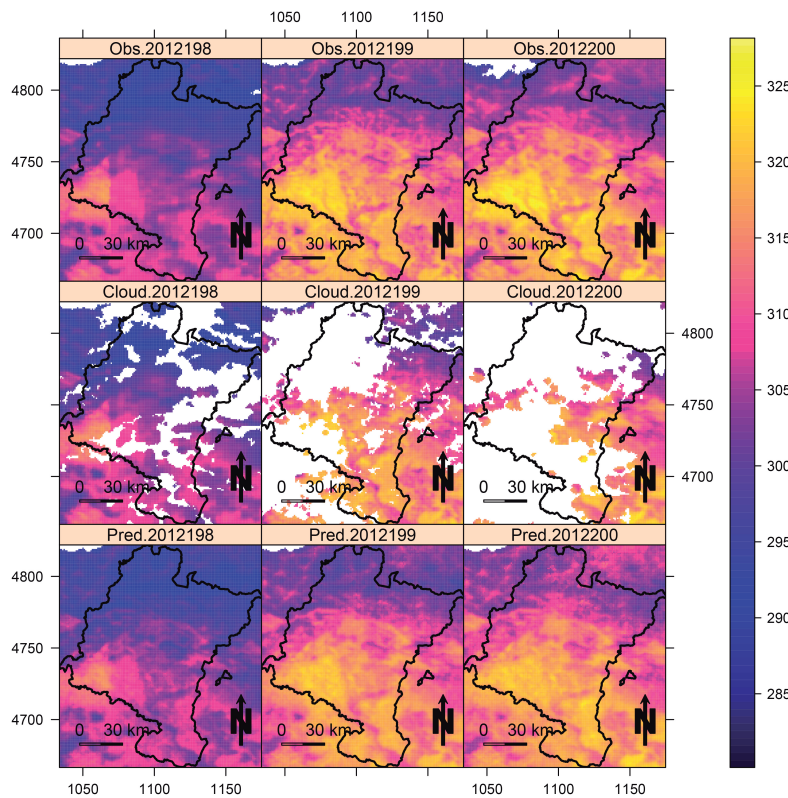


Fig. 7. First row shows the observed LST day target images (in Kelvin degrees) of the 16th (2012198), 17th (2012199), and 18th (2012200) of July 2012 in Navarre. The second row shows the same images masked with real clouds borrowed from the 3rd, 14th, and 21st of July 2011, respectively, and the third row shows the IMA predicted images.

evaluation of the RMSE is proposed. The RMSE is an indicator of the gap-filling fidelity because it has the same measurement units than the original variable, and it is very intuitive. Nevertheless, it can be calculated only when we know the ground-truth data, because then we can subtract the ground-truth data from the prediction. Simulation procedures make it possible because we know real data. Furthermore, a data set of

three target LST day and NDVI images using a neighborhood of 27 images was created for illustrating the performance of IMA with regard to GF algorithm. Overall, both the simulation study and the real data proved the outperformance of the IMA method.

As for computing time, Table VII shows the running times required for processing 5796 images. They correspond to

TABLE VII
 RUNNING TIMES IN MINUTES (M) AND HOURS (H) WHEN
 PROCESSING 138 LST DAY TIME SERIES OF 1 KM²
 RESOLUTION IMAGES IN NAVARRE WITH HANTS, THE
 TREE VERSIONS OF TIMESAT, GF, AND IMA

	Hants	Timesat			Gapfill	IMA	
		DL	AG	SG			
Pre-process	1m	2m	2m	2m	1m	0m	
Configuration	5m	10m	10m	10m	0m	0m	
Running time	Type A	2m	2m	2m	2m	27m	35m
	Type B	2m	2m	2m	2m	59m	35m
	Type C	2m	2m	2m	2m	1h 3m	34m
	Type D	2m	2m	2m	2m	2h 10m	31m
	Type E	2m	2m	2m	2m	11h 20m	29m
	Type F	2m	2m	2m	2m	20h 2m	26m
	Type G	2m	2m	2m	2m	1d 6h 13m	21m
Export to TIFF	2m	6m	6m	6m	1m	0m	
Total time	21m	31m	31m	31m	2d 17h 16m	3h 31m	

138 different LST day images processed with all methods, and different sizes of artificial clouds on a Windows PC with an Intel Core i7-4790, and 16 GB of RAM. Hants and Timesat are really fast, but GF is slowed down by its ranking process. The IMA method maintains a constant running time for both small and large gaps in the data and is faster than GF when processing moderate or large gaps. Though it is not as fast as Timesat or Hants, IMA processes the target images in less than 14 s on average, regardless of the gap size.

The filling process of both Timesat and Hants requires a moderate number of contiguous images from the same or, if the studied time period is at the very beginning or end of a year, the neighboring year, but GF and IMA need just a few images from previous and subsequent years to process the target image. However, Timesat and Hants smooth all the images in a row, because all images in the same time series become target images, while GF needs only a neighborhood to fill one target image, and IMA uses the same neighborhood for filling several images. Timesat and Hants programs smooth the time series of target images regardless of the presence of gaps or not. However, gaps that must be filled need to be identified prior to processing in GF and IMA. Usually, they are identified as missing data. GF fills the empty pixels of the target image one by one, and IMA fills simultaneously all the pixels of the target image. GF and IMA take profit of the temporal dependence using the next and previous images across the years in a neighborhood, where great similarities are expected. GF incorporates the spatial dependence among remote sensing data when ranking nearby pixels, and IMA when averaging, and interpolating the anomalies. The shortcomings of Timesat and Hants are the tuning constants and the input parameters that must be configured. Their advantages come from their short running time, and the extraction of seasonality parameters made by Timesat.

The IMA procedure also provides the standard errors of the anomalies when adding the option *fun=predictSE* from *fields* package [57] in the *interpolate* command. The approximation is borrowed from the kriging version of *Tps* function, and it assumes that the covariance parameters are already known. Hence, computing time for running IMA could increase substantially, because standard errors are calculated by default for every pixel of the target image. Processing the 27 images

of the real example takes less than 40 s, but calculating standard errors of only one image can last 10 min in a one thread computing and 5 min in a multithreading computing. The reason could be that the *predictSE* option is a linear approximation function that is not optimized for rasters. An alternative for reducing it is calculating the standard errors in a lower resolution raster, because estimates are fairly similar across the tile. For example, with an aggregation of factor 8, IMA takes on average 2 min to process the standard errors of one image.

Gerber *et al.* [16] distinguish four steps in the uncertainty estimation, but in the end only a combination of the 5–95 percentile prediction intervals of steps 2 and 3 is provided, because these steps dominate the uncertainty contributions, and adding all steps hardly increase the estimation of the prediction intervals. Computer time of the procedure is slightly increased. GF takes 1 h 45 min for gap-filling 27 images, including the prediction intervals, and can be reduced to 1 h 30 min when it does not estimate them. This time is obtained for a one thread computing in a PC with an Intel Core i7-4790, and 16 GB of RAM.

Simultaneous comparison of IMA and GF uncertainty measures is then a difficult task because both procedures provide different uncertainty measures (standard errors and prediction intervals), and the methodologies are completely different.

Cloud-filling methods have some limitations. For example, clouds that are found in the same locations across neighboring images in a systematic and periodic way could hinder efficient filling of gaps. Larger clouds cause estimation methods to lose robustness and become unstable. In those cases, wider neighborhoods are required in IMA, and likely programming improvements based on distributed programming and parallelizing are also necessary when input images are of high resolution. The independent steps required for running IMA can be easily fitted in the map reduce theory [61], and used in Hadoop cluster [62]. We are currently dealing with these issues.

VII. CONCLUSION

The IMA method assumes that remote sensing data can be expressed as the sum of a trend plus a random error. The trend is assumed to be constant in the neighborhood of the target image, and it is estimated with the mean of this neighborhood, and the residuals or anomalies are the estimates of the random error. Using repeated measurements from the same and contiguous time periods across several years provides a more robust estimation of the mean. Anomalies need to be filtered because images are not always free of altered or distorted data. Shrinking spatial resolution of the filtered anomalies is also a necessary step to reduce the dimension of the equations to be solved in the thin-plate splines and to mitigate the border effect. After interpolating the averaged anomalies, the new predictions are added to the mean image.

The IMA method is competitive for several reasons: 1) it shows a strong agreement between the benchmark image and the filled image; 2) it preserves the inherent phenology of the remote sensing data by estimating the mean of the same time periods in different years; 3) neither the tuning constant

nor any other parameter in the input configuration need to be specified in advance; 4) its image-processing runtime is consistent regardless of the data-gap size to be filled; 5) it exploits the benefits of the spatio-temporal dependence among time series of images; and 6) it is easy to use. The simulation study reveals that IMA outperforms Timesat, Hants, and GF, by reducing the RMSE for all three variables that were tested (LST Day, LST Night, and NDVI). The real case study also exhibits a good performance of IMA versus GF, particularly when filling daily LST day images.

ACKNOWLEDGMENT

The authors would like to thank the Editor-in-Chief S. Yueh and the comments made by the reviewers leading to an improvement of their paper upon the original submission.

REFERENCES

- [1] Y. Gao, H. Xie, T. Yao, and C. Xue, "Integrated assessment on multi-temporal and multi-sensor combinations for reducing cloud obscuration of MODIS snow cover products of the Pacific Northwest USA," *Remote Sens. Environ.*, vol. 114, no. 8, pp. 1662–1675, 2010.
- [2] H. Xie, X. Wang, and T. Liang, "Development and assessment of combined Terra and Aqua snow cover products in Colorado Plateau, USA and northern Xinjiang, China," *J. Appl. Remote Sens.*, vol. 3, no. 1, 2009, Art. no. 033559.
- [3] G. Yang, H. Shen, L. Zhang, Z. He, and X. Li, "A moving weighted harmonic analysis method for reconstructing high-quality SPOT VEGETATION NDVI time-series data," *IEEE Trans. Geosci. Remote Sens.*, vol. 53, no. 11, pp. 6008–6021, Nov. 2015.
- [4] H. Müller, P. Rufin, P. Griffiths, A. J. B. Siqueira, and P. Hostert, "Mining dense Landsat time series for separating cropland and pasture in a heterogeneous Brazilian savanna landscape," *Remote Sens. Environ.*, vol. 156, pp. 490–499, Jan. 2015.
- [5] A. Schneider, "Monitoring land cover change in urban and peri-urban areas using dense time stacks of Landsat satellite data and a data mining approach," *Remote Sens. Environ.*, vol. 124, pp. 689–704, Sep. 2012.
- [6] J. G. Masek *et al.*, "A Landsat surface reflectance dataset for North America, 1990–2000," *IEEE Geosci. Remote Sens. Lett.*, vol. 3, no. 1, pp. 68–72, Jan. 2006.
- [7] J. G. Masek *et al.*, "United States forest disturbance trends observed using Landsat time series," *Ecosystems*, vol. 16, no. 6, pp. 1087–1104, 2013.
- [8] Q. Meng, B. E. Borders, C. J. Cieszewski, and M. Madden, "Closest spectral fit for removing clouds and cloud shadows," *Photogramm. Eng. Remote Sens.*, vol. 75, no. 5, pp. 569–576, 2009.
- [9] X. Zhu, F. Gao, D. Liu, and J. Chen, "A modified neighborhood similar pixel interpolator approach for removing thick clouds in Landsat images," *IEEE Geosci. Remote Sens. Lett.*, vol. 9, no. 3, pp. 521–525, May 2012.
- [10] T. Hermosilla, M. A. Wulder, J. C. White, N. C. Coops, and G. W. Hobart, "An integrated Landsat time series protocol for change detection and generation of annual gap-free surface reflectance composites," *Remote Sens. Environ.*, vol. 158, pp. 220–234, Mar. 2015.
- [11] D. P. Roy *et al.*, "Multi-temporal MODIS–Landsat data fusion for relative radiometric normalization, gap filling, and prediction of Landsat data," *Remote Sens. Environ.*, vol. 112, no. 6, pp. 3112–3130, 2008.
- [12] B. Chen, B. Huang, L. Chen, and B. Xu, "Spatially and temporally weighted regression: A novel method to produce continuous cloud-free Landsat imagery," *IEEE Trans. Geosci. Remote Sens.*, vol. 55, no. 1, pp. 27–37, Jan. 2017.
- [13] L. Eklundh and P. Jönsson, *TIMESAT 3.2 With Parallel Processing-Software Manual*. Lund, Sweden: Lund Univ., 2012.
- [14] W. Verhoef, M. Menenti, and S. Azzali, "Cover A colour composite of NOAA-AVHRR-NDVI based on time series analysis (1981–1992)," *Int. J. Remote Sens.*, vol. 17, no. 2, pp. 231–235, 1996.
- [15] G. J. Roerink, M. Menenti, and W. Verhoef, "Reconstructing cloudfree NDVI composites using Fourier analysis of time series," *Int. J. Remote Sens.*, vol. 21, no. 9, pp. 1911–1917, 2000.
- [16] F. Gerber, R. de Jong, M. E. Schaepman, G. Schaepman-Strub, and R. Furrer, "Predicting missing values in spatio-temporal remote sensing data," *IEEE Trans. Geosci. Remote Sens.*, vol. 56, no. 5, pp. 2841–2853, May 2018.
- [17] F. Gerber, R. Furrer, G. Schaepman-Strub, R. de Jong, and M. E. Schaepman. (2016). "Predicting missing values in spatio-temporal satellite data." [Online]. Available: <https://arxiv.org/abs/1605.01038>
- [18] M. F. Hutchinson and P. E. Gessler, "Splines—More than just a smooth interpolator," *Geoderma*, vol. 62, nos. 1–3, pp. 45–67, 1994.
- [19] A. F. Militino, M. D. Ugarte, and U. Pérez-Goya, "Improving the quality of satellite imagery based on ground-truth data from rain gauge stations," *Remote Sens.*, vol. 10, no. 3, p. 398, 2018.
- [20] J. C.-W. Chan, J. Ma, P. Kempeneers, and F. Canters, "Superresolution enhancement of hyperspectral CHRIS/Proba images with a thin-plate spline nonrigid transform model," *IEEE Trans. Geosci. Remote Sens.*, vol. 48, no. 6, pp. 2569–2579, Jun. 2010.
- [21] X. Zhang *et al.*, "Local adaptive calibration of the satellite-derived surface incident shortwave radiation product using smoothing spline," *IEEE Trans. Geosci. Remote Sens.*, vol. 54, no. 2, pp. 1156–1169, Feb. 2016.
- [22] Y. Jin, Y. Ge, J. Wang, Y. Chen, G. B. Heuvelink, and P. M. Atkinson, "Downscaling amsr-2 soil moisture data with geographically weighted area-to-area regression Kriging," *IEEE Trans. Geosci. Remote Sens.*, vol. 56, no. 4, pp. 2362–2376, Apr. 2018.
- [23] A. Verdin, C. Funk, B. Rajagopalan, and W. Kleiber, "Kriging and local polynomial methods for blending satellite-derived and gauge precipitation estimates to support hydrologic early warning systems," *IEEE Trans. Geosci. Remote Sens.*, vol. 54, no. 5, pp. 2552–2562, May 2016.
- [24] G. Matheron, "Splines and Kriging: Their formal equivalence," in *Down-to-Earth-Statistics: Solutions Looking for Geological Problems*. Syracuse, NY, USA: Syracuse University Geological Contributions, 1981, pp. 77–95.
- [25] M. L. Stein, "A kernel approximation to the Kriging predictor of a spatial process," *Ann. Inst. Stat. Math.*, vol. 43, no. 1, pp. 61–75, 1991.
- [26] N. Cressie and C. K. Wikle, *Statistics for Spatio-Temporal Data*. Hoboken, NJ, USA: Wiley, 2015.
- [27] R. E. Rossi, J. L. Dungan, and L. R. Beck, "Kriging in the shadows: Geostatistical interpolation for remote sensing," *Remote Sens. Environ.*, vol. 49, no. 1, pp. 32–40, 1994.
- [28] E. Addink, "A comparison of conventional and geostatistical methods to replace clouded pixels in NOAA-AVHRR images," *Int. J. Remote Sens.*, vol. 20, no. 5, pp. 961–977, 1999.
- [29] J. N. Hird and G. J. McDerimid, "Noise reduction of NDVI time series: An empirical comparison of selected techniques," *Remote Sens. Environ.*, vol. 113, no. 1, pp. 248–258, 2009.
- [30] P. F. Velleman, "Definition and comparison of robust nonlinear data smoothing algorithms," *J. Amer. Statist. Assoc.*, vol. 75, no. 371, pp. 609–615, 1980.
- [31] M. Ma and F. Veroustraete, "Reconstructing pathfinder AVHRR land NDVI time-series data for the Northwest of China," *Adv. Space Res.*, vol. 37, no. 4, pp. 835–840, 2006.
- [32] D. Filipova-Racheva and M. Hall-Beyer, "Smoothing of NDVI time series curves for monitoring of vegetation changes in time," in *Proc. Ecological Monitor. Assessment Netw. Nat. Sci. Meeting*, 2000, pp. 17–22.
- [33] J. Zhou, L. Jia, and M. Menenti, "Reconstruction of global MODIS NDVI time series: Performance of Harmonic ANalysis of Time Series (HANTS)," *Remote Sens. Environ.*, vol. 163, pp. 217–228, Jun. 2015.
- [34] L. Poggio, A. Gimona, and I. Brown, "Spatio-temporal MODIS EVI gap filling under cloud cover: An example in Scotland," *ISPRS J. Photogram. Remote Sens.*, vol. 72, pp. 56–72, Aug. 2012.
- [35] J. Chen, X. Zhu, J. E. Vogelmann, F. Gao, and S. Jin, "A simple and effective method for filling gaps in Landsat ETM+ SLC-off images," *Remote Sens. Environ.*, vol. 115, no. 4, pp. 1053–1064, 2011.
- [36] M. Pringle, M. Schmidt, and J. Muir, "Geostatistical interpolation of SLC-off Landsat ETM+ images," *ISPRS J. Photogram. Remote Sens.*, vol. 64, no. 1, pp. 654–664, 2009.
- [37] X. Zhu, D. Liu, and J. Chen, "A new geostatistical approach for filling gaps in Landsat ETM+ SLC-off images," *Remote Sens. Environ.*, vol. 124, no. 1, pp. 49–60, 2012.
- [38] G. Yin, G. Mariethoz, and M. F. McCabe, "Gap-Filling of Landsat 7 imagery using the direct sampling method," *Remote Sens.*, vol. 9, no. 1, p. 12, 2016.
- [39] C. Strong and K. M. Golden, "Filling the polar data gap in sea ice concentration fields using partial differential equations," *Remote Sens.*, vol. 8, no. 6, p. 442, 2016.

- [40] P. M. Atkinson, C. Jeganathan, J. Dash, and C. Atzberger, "Inter-comparison of four models for smoothing satellite sensor time-series data to estimate vegetation phenology," *Remote Sens. Environ.*, vol. 123, pp. 400–417, Aug. 2012.
- [41] G. Yin, G. Mariethoz, Y. Sun, and M. F. McCabe, "A comparison of gap-filling approaches for Landsat-7 satellite data," *Int. J. Remote Sens.*, vol. 38, no. 23, pp. 6653–6679, 2017. doi: 10.1080/01431161.2017.1363432.
- [42] R. Liu, R. Shang, Y. Liu, and X. Lu, "Global evaluation of gap-filling approaches for seasonal NDVI with considering vegetation growth trajectory, protection of key point, noise resistance and curve stability," *Remote Sens. Environ.*, vol. 189, pp. 164–179, Feb. 2017.
- [43] J. M. Chen, F. Deng, and M. Chen, "Locally adjusted cubic-spline capping for reconstructing seasonal trajectories of a satellite-derived surface parameter," *IEEE Trans. Geosci. Remote Sens.*, vol. 44, no. 8, pp. 2230–2238, Aug. 2006.
- [44] (2017). MODIS. [Online]. Available: <https://modis.gsfc.nasa.gov/about/>
- [45] D. A. Slayback, J. E. Pinzon, S. O. Los, and C. J. Tucker, "Northern hemisphere photosynthetic trends 1982–99," *Global Change Biol.*, vol. 9, no. 1, pp. 1–15, 2003.
- [46] C. J. Tucker *et al.*, "An extended AVHRR 8-km NDVI dataset compatible with MODIS and SPOT vegetation NDVI data," *Int. J. Remote Sens.*, vol. 26, no. 20, pp. 4485–4498, 2005.
- [47] J. W. J. Rouse, R. H. Haas, J. Schell, and D. W. Deering, "Monitoring vegetation systems in the great plains with ERTS," *NASA Special Pub.*, vol. 351, p. 309, Jan. 1974.
- [48] M. T. van Wijk and M. Williams, "Optical instruments for measuring leaf area index in low vegetation: Application in arctic ecosystems," *Ecological Appl.*, vol. 15, no. 4, pp. 1462–1470, 2005.
- [49] A. Benali, A. C. Carvalho, J. P. Nunes, N. Carvalhais, and A. Santos, "Estimating air surface temperature in Portugal using MODIS LST data," *Remote Sens. Environ.*, vol. 124, pp. 108–121, Sep. 2012.
- [50] Z. Wan and J. Dozier, "A generalized split-window algorithm for retrieving land-surface temperature from space," *IEEE Trans. Geosci. Remote Sens.*, vol. 34, no. 4, pp. 892–905, Jul. 1996.
- [51] Z. Wan, Y. Zhang, Q. Zhang, and Z.-L. Li, "Validation of the land-surface temperature products retrieved from terra moderate resolution imaging spectroradiometer data," *Remote Sens. Environ.*, vol. 83, nos. 1–2, pp. 163–180, Nov. 2002.
- [52] S. N. Wood, "Thin plate regression splines," *J. Roy. Statist. Soc. B (Statist. Methodol.)*, vol. 65, no. 1, pp. 95–114, Feb. 2003.
- [53] J. Li and A. D. Heap, "A review of comparative studies of spatial interpolation methods in environmental sciences: Performance and impact factors," *Ecological Informat.*, vol. 6, nos. 3–4, pp. 228–241, 2011.
- [54] W. Luo, M. C. Taylor, and S. R. Parker, "A comparison of spatial interpolation methods to estimate continuous wind speed surfaces using irregularly distributed data from England and Wales," *Int. J. Climatol.*, vol. 28, no. 7, pp. 947–959, 2008.
- [55] J. Duchon, "Splines minimizing rotation-invariant semi-norms in Sobolev spaces," in *Constructive Theory of Functions of Several Variables*. Berlin, Germany: Springer, 1977, pp. 85–100.
- [56] E. P. J. Boer, K. M. de Beurs, and A. D. Hartkamp, "Kriging and thin plate splines for mapping climate variables," *Int. J. Appl. Earth Observ. Geoinformation*, vol. 3, no. 2, pp. 146–154, 2001.
- [57] D. Nychka, R. Furrer, J. Paige, and S. Sain. (2015). FIELDS: Tools for Spatial Data. University Corporation for Atmospheric Research, Boulder, CO, USA. [Online]. Available: www.image.ucar.edu/fields
- [58] M. Neteler and H. Mitasova, *Open Source GIS: A GRASS GIS Approach*, vol. 689. Luxembourg: Springer, 2013.
- [59] R. C. Team. (2018). R: A Language Environment for Statistical Computing. R Foundation for Statistical Computing. Vienna, Opera, Austria. [Online]. Available: <https://www.R-project.org/>
- [60] C. Davino, M. Furno, and D. Vistocco, *Quantile Regression: Theory and Applications*. Hoboken, NJ, USA: Wiley, 2013.
- [61] J. Leskovec, A. Rajaraman, and J. D. Ullman, *Mining of Massive Datasets*. Cambridge, U.K.: Cambridge Univ. Press, 2014.
- [62] (2009). *Apache Hadoop*. [Online]. Available: <http://hadoop.apache.org>



Ana F. Militino received the M.Sc. degree in mathematics from the University of Zaragoza, Zaragoza, Spain, in 1981, and the Ph.D. degree in statistics from the University of Extremadura, Badajoz, Spain, in 1984.

She is currently a Full Professor of statistics with the Statistics, Computer Science and Mathematics Department, Public University of Navarre, Pamplona, Spain. She has co-authored *Probability and Statistics With R* (CRC Press/Taylor and Francis, 1st Ed., 2008 and 2nd Ed., 2015). Her research inter-

ests include spatial statistics, spatio-temporal statistics, and remote sensing. She has authored or co-authored numerous papers in these areas.

Dr. Militino was a recipient of the John Griffiths Teaching Award by the International Association of Mathematical Geology in 2010. She has also participated in a large number of research projects sponsored by the Spanish Ministry of Education and Science, Agriculture, Navarre Statistical Institute, Basque Country Statistical Institute, and other private companies.



M. Dolores Ugarte received the M.Sc. degree in mathematics from the University of Zaragoza, Zaragoza, Spain, in 1989, and the Ph.D. degree in statistics from the Public University of Navarre, Pamplona, Spain, in 1996.

She is currently a Full Professor of statistics with the Statistics, Computer Science and Mathematics Department, Public University of Navarre. Her research interests include spatial statistics, spatio-temporal statistics, remote sensing, and disease mapping.

Dr. Ugarte is currently a member of the Executive Committee of the Federation of European National Statistical Societies (FenSTATs). She is currently the Co-Editor-in-Chief of the Journal *TEST*, an Associate Editor of *Statistical Modelling*, and a member of the board of the *Spatial and Spatio-Temporal Epidemiology*. She is the Coordinator of mathematical projects in the Spanish Research Agency and the Principal Investigator of several projects of the Spanish Ministry of Economy, Industry and Competitiveness.



Unai Pérez-Goya received the B.Sc. degree in computer science engineering from the University of Mondragón, Mondragón, Spain, in 2012, and the master's degree in innovation and research in informatics (MIRI) from the Polytechnic University of Catalonia, Barcelona, Spain, in 2015. He is currently pursuing the Ph.D. degree in science and industrial technologies with the Public University of Navarra, Pamplona, Spain, under the supervision of A. F. Militino and M. D. Ugarte.



Marc G. Genton received the M.Sc. degree in applied mathematics from the Swiss Federal Institute of Technology, Zürich, Switzerland, in 1992, and the Ph.D. degree in statistics from the Swiss Federal Institute of Technology (EPFL), Lausanne, Switzerland, in 1996.

He is currently a Distinguished Professor of statistics with the King Abdullah University of Science and Technology, (KAUST), Thuwal, Saudi Arabia. His research interests include statistical analysis, modeling, prediction, and uncertainty quantification

of spatio-temporal data, with applications in environmental and climate science, renewable energies, geophysics, and marine science.